OpenLSA: An open-source toolbox for computing full-field displacements from images of periodic patterns

Benoît Blaysat, Frédéric Sur, Thomas Jailin, Adrien Vinel, Michel Grédiac

SoftwareX 27 (2024) 101826

Contents lists available at ScienceDirect

SoftwareX

journal homepage: www.elsevier.com/locate/softx

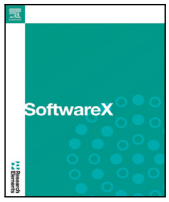

Original software publication

OpenLSA: An open-source toolbox for computing full-field displacements from images of periodic patterns

Benoît Blaysat [a,b,*], Frédéric Sur [c], Thomas Jailin [a], Adrien Vinel [a], Michel Grédiac [a]

[a] Université Clermont Auvergne, CNRS, Clermont Auvergne INP, Institut Pascal, F-63000, Clermont-Ferrand, France
[b] Institut Universitaire de France, Paris, France
[c] LORIA, Université de Lorraine, CNRS, INRIA, Nancy, BP 239, F-54506, France

ARTICLE INFO

Dataset link: https://github.com/BenoitBlaysat/OpenLSA.git

Keywords:
Experimental mechanics
Full-field measurements
Digital image correlation
Localized spectrum analysis

ABSTRACT

In the experimental mechanics community, full-field measurement techniques have gained popularity over the last few decades, revolutionizing traditional testing procedures for materials and structures. While Digital Image Correlation (DIC) remains the most widely used method, its reliance on randomly patterned surfaces limits its metrological performance, and the iterative calculations required for retrieving displacement and strain fields can be computationally expensive. In recent years, there has been a proposal to use optimal checkerboard patterns instead. Images of such periodic patterns can be processed using a method called Localized Spectrum Analysis (LSA). LSA proposes processing these images in the frequency domain using spectral techniques, which reduces computational costs. This paper presents an open-source LSA software written in Python and illustrates two application cases in experimental mechanics.

Code metadata

Current code version	v0.9.8
Permanent link to code/repository used for this code version	https://github.com/ElsevierSoftwareX/SOFTX-D-24-00184
Permanent link to Reproducible Capsule	https://codeocean.com/capsule/4304074/tree
Legal Code License	GNU General Public License (GPL)
Code versioning system used	git
Software code languages, tools, and services used	python
Compilation requirements, operating environments & dependencies	python librairies: numpy, scipy, scikit-image, opencv-python, pillow, matplotlib, boto3
If available Link to developer documentation/manual	https://github.com/BenoitBlaysat/OpenLSA/blob/main/README.md
Support email for questions	benoit.blaysat@uca.fr

1. Motivation and significance

In experimental mechanics, devices providing full-field kinematic data are nowadays routinely used. They mostly rely on cameras that take images of the surface texture of a specimen, the latter being subjected to thermal and/or mechanical loads. Image processing is then performed to retrieve the displacements at every pixel from the stack of images. Considering planar specimens, such displacement maps make it possible to observe the different mechanisms that operate in the specimen properly. Modeling these mechanisms and identifying the material constitutive behavior become then easier. It is worth noting that the elastic domain is often investigated. This usually leads to strain magnitude below 10^{-3} [-]. Digital Image Correlation (DIC) is the most common image processing technique used to determine the displacement field from a pair of images [1]. It identifies that displacement field by iteratively minimizing the optical residual. In its simplest form, this quantity represents the squared difference of the gray level distributions estimated over small subsets selected in the reference and current images, the latter image being mapped onto the former through the sought displacement. Numerous software are available, including both open-source versions [2–5] or commercial versions [6–8]. These

* Corresponding author at: Université Clermont Auvergne, CNRS, Clermont Auvergne INP, Institut Pascal, F-63000, Clermont-Ferrand, France.
E-mail address: benoit.blaysat@uca.fr (Benoît Blaysat).

https://doi.org/10.1016/j.softx.2024.101826
Received 26 March 2024; Received in revised form 9 July 2024; Accepted 10 July 2024
Available online 23 July 2024

examples illustrate the diversity of available software, but it should be noted that this is not a comprehensive list.

For the experimental mechanics community, challenges addressed by full-field measurement tools mainly involve: (i) the reduction of the computing time required for calculating the displacement maps, and (ii) the optimization of the metrological performance associated with the measurement. Both challenges have been widely addressed in the literature.

For instance, Computing time has been reduced through the implementation of DIC on Graphics Processor Units [9,10]. Nevertheless, DIC is an iterative process. It remains, by nature, computationally intensive. More recently, the problem has been reformulated through the use of a dedicated Convolutional Neural Network [11,12].

The assessment and the optimization of the metrological performance of DIC tools is a topical subject [13–40]. The community now acknowledges that enhancing the metrological performance requires paying closer attention to the image pattern. In the early ages of DIC, ease of implementation was considered paramount. Speckle textures obtained with spray paint were then commonly used for this purpose, given random features that prevented DIC from getting trapped in local minima. However, the demand for accurate measurements now compels DIC users to accurately formulate rules regarding pattern texture in DIC measurements. Checkerboard patterns appear optimal for obtaining measurements with the highest metrological performance [29,41]. Nevertheless, DIC users generally do not employ such patterns because of their periodicity, which causes classic DIC algorithms to be entrapped in local minima. Some studies state that patterns should ideally be "similar to" a checkerboard, but "sufficiently random" to avoid the above-mentioned issue [42].

Localized Spectrum Analysis (LSA) is one of the techniques developed to extract displacement fields from images of periodic patterns. It presents interesting properties in this context. First, this is a spectral approach that minimizes the optical residual in the Fourier domain, thus drastically reducing the computing cost of displacement calculations [43]. Second, it can easily process checkerboard images and other types of periodic patterns such as 2D grids.

The present paper aims to introduce a new software, OpenLSA. It is the culmination of developments over the last decade in collaboration between LORIA, (Université de Lorraine, Nancy, France) and the "Experimental Mechanics" team of the Institut Pascal research group, Clermont-Ferrand, France. LSA has been utilized in numerous papers dealing with material and structure characterization [35,43–53]. However, only an early Matlab software toolbox [54] based on this technique is available, which justifies the present contribution developed with Python.

2. Software description

2.1. Properties of images of periodic patterns

The images considered here exhibit specific properties. They consist of multiple repetitions of an initial pattern, arranged with a given period along two perpendicular directions. An illustration is provided in Fig. 1. Fig. 1(a) depicts an imaged specimen surface, on which a checkerboard has been engraved following the procedure detailed in [47]. On a white background, the unit cell of the pattern consists here of a black shape of width about 30 [μm]. This pattern is then repeated along the perpendicular directions $(\underline{e}_\alpha, \underline{e}_\beta)$ of the square with the period $p = 30\sqrt{2}$ [μm], as illustrated by the close-up in Fig. 1(b). The acquired image by the camera sensor can thus be modeled as the summation of two perpendicular *1D*-periodic signals. In practice, the wave vector $\underline{k}$, defined for both α and β directions, uniquely characterizes the direction and the period of such a signal. Specifically, its period corresponds to the inverse of the norm of the wave vector, *i.e.* $p = 1/\|\underline{k}\|$ and the repetition direction is given by the vector direction.

2.2. Brief reminder of LSA basics

2.2.1. Displacement measurement with periodic patterns

The present paragraph presents the modeling of images of checkerboard patterns, possibly deformed. The undeformed checkerboard is assumed to be made of square patterns. Let I^0 (resp. I^t) be the gray level intensities of the reference image (resp. current image). It satisfies at any pixel location $\underline{\mathrm{x}}$, $\forall i \in \{0,t\}$,

$$\mathrm{I}^i(\underline{\mathrm{x}}) = \mathtt{frng}\left(2\pi\underline{k}_\alpha \cdot \underline{\mathrm{x}} + \varphi^i_\alpha(\underline{\mathrm{x}})\right) + \mathtt{frng}\left(2\pi\underline{k}_\beta \cdot \underline{\mathrm{x}} + \varphi^i_\beta(\underline{\mathrm{x}})\right), \tag{1}$$

where "frng" is a 2π periodic function, $\underline{k}_\alpha$ (resp. $\underline{k}_\beta$) is the wave vector of the pattern periodicity and $\underline{e}_\alpha$ (resp. $\underline{e}_\beta$) is the unit vector such that $\underline{e}_\ell = \underline{k}_\ell/\|\underline{k}_\ell\|$, $\forall \ell \in \{\alpha,\beta\}$. With checkboard patterns, the directions of the pattern periodicity $\underline{e}_\alpha$ and $\underline{e}_\beta$ are orthogonal. $(\varphi^0_\ell, \varphi^t_\ell)_{\ell\in\{\alpha,\beta\}}$ are the phase modulations of the reference and the current configurations, of the two perpendicular signals forming the checkerboard pattern [53], and finally "$\cdot$" is the 2D Euclidean dot product.

Denoting by $\underline{u}$ the displacement field that warps the reference image I^0 to the current image I^t, the conservation of the optical flow writes:

$$\mathrm{I}^0(\underline{\mathrm{x}}) = \mathrm{I}^t(\underline{\mathrm{x}} + \underline{u}(\underline{\mathrm{x}})). \tag{2}$$

After identification of the phase modulations of the "frng" functions, the above equation leads to, $\forall \ell \in \{\alpha,\beta\}$:

$$2\pi\underline{k}_\ell \cdot \underline{\mathrm{x}} + \varphi^0_\ell(\underline{\mathrm{x}}) = 2\pi\underline{k}_\ell \cdot (\underline{\mathrm{x}} + \underline{u}(\underline{\mathrm{x}})) + \varphi^t_\ell(\underline{\mathrm{x}} + \underline{u}(\underline{\mathrm{x}})). \tag{3}$$

Hence, since $(\underline{e}_\alpha, \underline{e}_\beta)$ defines an orthonormal basis, the displacement satisfies:

$$\underline{u}(\underline{\mathrm{x}}) = \sum_{\ell=\{\alpha,\beta\}} \frac{\varphi^0_\ell(\underline{\mathrm{x}}) - \varphi^t_\ell(\underline{\mathrm{x}} + \underline{u}(\underline{\mathrm{x}}))}{2\pi\|\underline{k}_\ell\|}\underline{e}_\ell, \tag{4}$$

where $\|\cdot\|$ denotes the Euclidean norm of vector $\}\cdot\varepsilon$. These phase modulations may be caused by any global translation or local deviation from a perfect periodic pattern, typically displacement for the latter.

2.2.2. Extraction of the raw phase modulations

From an image I^i with $i \in \{0,t\}$, an estimation of the phase modulations $(\varphi^i_\ell)_{\ell\in\{1,2\}}$ is obtained, at first order, by calculating the arguments of the windowed discrete Fourier transform (WDFT) at the frequencies and directions of each wave carrier [55]. Let $\mathsf{F}_{w_\sigma}(\mathrm{I})$ be to the windowed discrete Fourier transform of image I with the Gaussian window of standard deviation σ denoted by w_σ:

$$\mathsf{F}_{w_\sigma}(\mathrm{I})(\underline{\mathrm{x}},\underline{k}) = \sum_{\underline{x}} w_\sigma(\underline{x}-\underline{\mathrm{x}})\mathrm{I}(\underline{x})e^{-2j\pi\underline{k}\cdot\underline{x}}. \tag{5}$$

with $w_\sigma(\underline{x}) = 1/(2\pi\sigma^2)e^{-\|\underline{x}\|/(2\sigma^2)}$ and j is the imaginary unit defined by $j^2 = -1$. The pros and cons of different windows are discussed in [56] and the conclusion is that the Gaussian window leads to the best trade-off.

Hence, the phase modulation writes, $\forall \ell \in \{\alpha,\beta\}$, $\forall i \in \{0,t\}$

$$\varphi^i_\ell(\underline{\mathrm{x}}) \approx \mathrm{angle}\left(\mathsf{F}_{w_\sigma}(\mathrm{I})(\underline{\mathrm{x}},\underline{k}_\ell)\right) + 2\pi\mathrm{c}^i_\ell(\underline{\mathrm{x}}), \tag{6}$$

where functions c^i_ℓ, which return signed integers for any pixels, are introduced to correct the 2π-jumps of the "angle" function, because the latter is giving the argument of any complex number, defined up to 2π.

2.2.3. Unwrapping the raw phase modulations

The calculation of functions c^i_ℓ is depicted with an academic illustration in Fig. 2. Let us consider a 1D problem consisting of a 1D specimen subjected to a uniform stretch of 5% strain. The corresponding displacement is shown in Fig. 2(a). This displacement is equal to 0 [px] at the center of the studied domain, *i.e.* for $x = 100$ [px] here. The phase modulation associated with such a displacement, considering a wave carrier of 5 [px] period, is also displayed. In this particular case, we assume the pattern to be perfectly encoded; consequently, the phase modulation of the reference state is null.

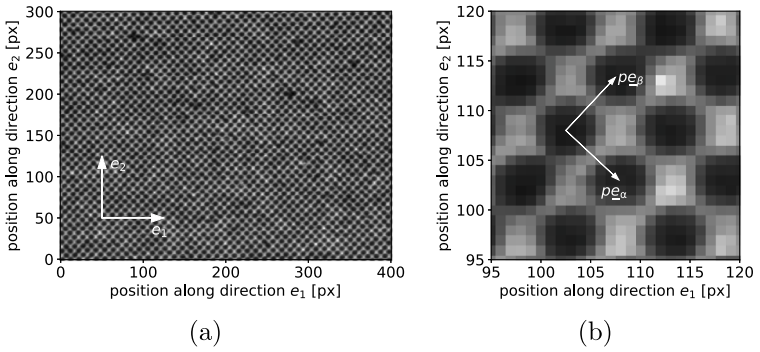

Fig. 1. Illustration of an image of a periodic pattern. A checkerboard has been deposited onto a specimen surface. (a) image of the specimen surface; (b) Close-up view of the image (a).

Applying 1D LSA to the 1D deformed pattern provides the raw phase modulation plotted in Fig. 2(b). However, the angle of a complex number is defined *modulo* 2π. Hence, two phenomena are induced.

- First, the angle of the WDFT is often spatially wrapped, so spatial unwrapping must be performed. This spatial unwrapping consists of adding pixel-wise integer multiple of 2π, so that the 2π-jumps of wrapped maps are removed. $(\mathrm{c}^i_\ell)_{i\in\{0,t\},\ell\in\{1,2\}}$ maps collect these pixel-wise integers, as illustrated in Fig. 2(c) for the considered 1D case.
- Second, the unwrapped phase maps are obtained *modulo* 2π, with the same multiple of 2π for all the pixels. A pairing is, therefore, performed between the reference and current phase modulations to obtain the value of this multiple. Plugging Eq. (6) into Eq. (3) gives, $\forall \ell \in \{\alpha, \beta\}$:

$$\underline{k}_\ell \cdot \underline{u}(\underline{\mathrm{x}}) = \frac{\tilde{\varphi}^0_\ell(\underline{\mathrm{x}}) - \tilde{\varphi}^t_\ell(\underline{\mathrm{x}} + \underline{u}(\underline{\mathrm{x}}))}{2\pi} + \mathrm{c}^0_\ell(\underline{\mathrm{x}}) - \mathrm{c}^t_\ell(\underline{\mathrm{x}} + \underline{u}(\underline{\mathrm{x}}))$$
$$\text{with } \tilde{\varphi}^i_\ell(\underline{\mathrm{x}}) = \mathrm{angle}\left(\mathrm{F}_{w_\sigma}(\mathrm{I}^i)(\underline{\mathrm{x}}, \underline{k}_\ell)\right). \quad (7)$$

The pairing is calculated by assuming that the displacement $\underline{u}_0$ at a given specific location $\underline{\mathrm{x}}_0$ is known. In practice, $\underline{u}_0$ is obtained by tracking a marking defect. Indeed, Eq. (7) leads to

$$\mathrm{c}^t_\ell(\underline{\mathrm{x}}_0 + \underline{u}_0) = \mathrm{c}^0_\ell(\underline{\mathrm{x}}_0) + \left[\frac{\tilde{\varphi}^0_\ell(\underline{\mathrm{x}}_0) - \tilde{\varphi}^t_\ell(\underline{\mathrm{x}}_0 + \underline{u}_0)}{2\pi} - \underline{k}_\ell \cdot \underline{u}_0\right]. \quad (8)$$

The bracket notation refers to the rounding function to the nearest integer. This rounding is required because of numerical errors. Considering the 1D case, the correction function is adjusted such that the displacement $\underline{u}_0$, deduced from the phase modulation, equals 0 [px] at $\underline{x}_0 = 100$ [px], *i.e.* at the center of the domain. This is illustrated in Fig. 2(d).

2.2.4. Code overview

To summarize, the displacement estimation from a pair of images by LSA consists of

(i) extracting the wrapped phase modulations from images I^0 and I^t using Eq. (6);
(ii) computing functions $(\mathrm{c}^i_\ell(\underline{\mathrm{x}}))_{i\in\{0,t\},\ell\in\{1,2\}}$: spatially unwrapping all maps, and pairing the reference and current phase modulations based on the known displacement of a given point using Eq. (8);
(iii) solving Eq. (4) using a fixed-point algorithm, since the sought quantity $\underline{u}(\underline{\mathrm{x}})$ is involved in both parts of the equality.

The organigram in Fig. 3 illustrates the code flow.

2.3. Software architecture

The software was designed to be straightforward for easy comprehension. The aim is to enable researchers, even those with little programming experience, to read, understand, and modify the code easily if needed.

The `lsa` class is the main class of this software. The `__init__` method of this class initializes the problem. For any new case study, an image must be provided. The period and the orientation of the pattern, gathered in vector $\underline{k}$, are determined by the `__compute_vec_k` private method, which localizes the highest peak in the spectrum of the checkerboard image. The central peak is masked under the assumption that the pattern pitch is lower than `max_pitch`, which is set by default to 30 [pixels]. This corresponds to masking the central part of the spectrum: the pattern pitch is sought in the spectrum with a frequency larger than $1/$`max_pitch`. Similarly, a lower bound is also introduced, defined by the variable `min_pitch`, which is set by default to $2\sqrt{2}$ [px]. For a checkerboard, the pattern pitch corresponds to the diagonal of a white or black square. This default value thus encodes each square by 2×2 pixels, which reaches the lowest limit to avoid aliasing effects [57]. Once the highest peak is located, $\underline{k}_\alpha$ is defined. It is rotated by a multiple of $\pi/2$ to be as close as possible to the `init_angle` angle, which is set to 0 [rad] by default. The class constructor `__init__` initializes $\underline{k}_\alpha$ if an image is given; otherwise, $\underline{k}_\alpha$ must be provided by the user. $\underline{k}_\beta$ is then defined by rotating $\underline{k}_\alpha$ by $\pi/2$. $\underline{k}_\alpha$ and $\underline{k}_\beta$ define an attribute of the OpenLSA class, concatenated into the `vec_k` list.

After creating the class and defining the wave carriers, the window required for the WDFT needs to be elaborated. The `compute_kernel` method builds the Gaussian kernel with a standard deviation equal to `std`. `std` corresponds to σ in the previous section. If `std` is not provided, it is defined by default as the smallest acceptable value, *i.e.*, the period of the wave carriers [53].

At this stage, it is possible to compute the phase modulation for every image. This is the objective of the `compute_phases_mod` method. In practice, for each wave carrier direction $\underline{e}_\ell$, $\ell \in \{\alpha, \beta\}$, the method calculates the value of the angle taken by the WDFT of the checkerboard image at the corresponding frequency, *cf* Eq. (6). The modulus of the WFDT is also computed. It defines the region of interest `roi` if not provided. `roi` corresponds to the locations where the modulus of the WDFT is greater than an arbitrary value, set by default to a fifth of its maximum. The obtained phase modulations are subsequently unwrapped within the `roi`.

The `temporal_unwrap` method pairs phase modulations according to their corresponding images. To achieve this, a feature is extracted from the reference image, and its position defines a marker. This marker is then identified in the current image to facilitate pairing. The feature is usually a bright spot in a part of the pattern that exhibits correct encoding. Choosing a bright spot helps ensure that it is not caused by dust within the optical system. Since dust particles typically create black spots. The correct encoding of the pattern is determined by thresholding the modulus of the WDFT of the image at the pattern frequency by 75% of its maximum value. This ensures the selected

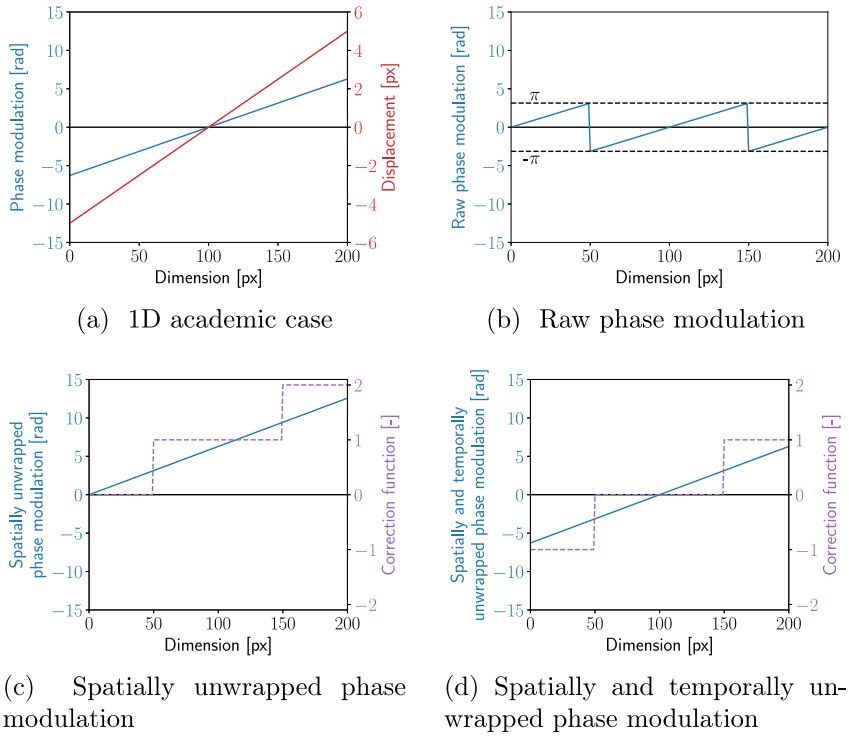

(a) 1D academic case (b) Raw phase modulation

(c) Spatially unwrapped phase modulation (d) Spatially and temporally unwrapped phase modulation

Fig. 2. Illustration of the spatial and temporal unwrapping necessary for the correct estimation of phase modulation. (a) 1D case: homogeneous stretching of a 1D sample. The displacement is affine, as is the associated phase modulation when considering a perfect pattern of 5 [px] period; (b) Raw wrapped phase modulation, obtained from the "angle" function applied to the WDFT of the stretched pattern; (c) Spatially unwrapped phase and its corresponding correction function; (d) Spatially and temporally unwrapped phase modulation, once the phase modulation of the stretched configuration has been paired to return the expected null displacement at the center of the specimen. The correction function is thus updated accordingly.

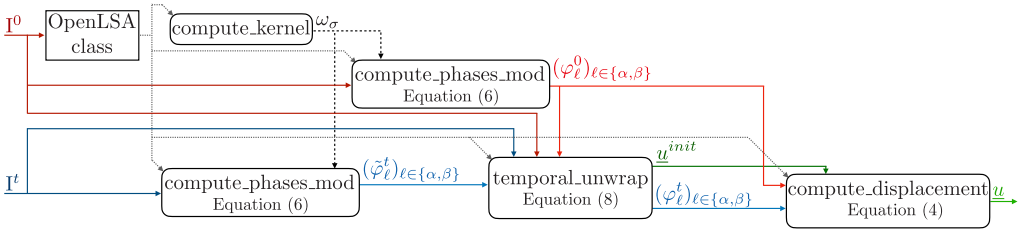

Fig. 3. Organigram of the code flow when OpenLSA is applied on an image pair $(\mathrm{I}^0, \mathrm{I}^t)$ to retrieve the displacement $\underline{u}$ that operates from the image I^0 to the image I^t.

feature is located far from the surface border and helps limit spot size, which could otherwise impair phase estimation. Two approaches to determining the marker location in the current image are implemented to limit incorrect pairing. Both methods utilize the OpenCV Python library. The first approach determines the displacement from the reference image to the current one by computing the corresponding optical flow, specifically using the Dense Inverse Search (DIS) algorithm. Blurring the images with a large kernel significantly smoothes the pattern to mitigate the influence of pattern periodicity, which could impede the DIS optical flow algorithm. The position of the marker in the current image is then computed using this displacement. The second approach finds the location that minimizes the normalized squared difference between the marker (size 30×30 pixels) and the current image. This calculation is carried out using the `matchTemplate` algorithm. If the positions of the markers differ by more than 1 [px], the one that results in the smallest sum of squared differences between the current image and the feature is kept. However, such an event generates a warning in the Python terminal during code execution. The pairing is then carried out by correcting the current phase modulation accordingly to Eq. (8).

Finally, the `compute_displacement` method solves Eq. (4) at each pixel of the region of interest. The displacement is defined as a complex number. The real (resp. imaginary) part corresponds to the displacement along the $\underline{e}_1$ (resp. $\underline{e}_2$) direction. A fixed-point algorithm is implemented for this purpose. The associated stopping criterion, defined by the average of the Euclidean norm of iterative corrections, is set by default to 5×10^{-4}. Moreover, the iterative process is stopped when the number of iterations reaches the value specified by `max_iter`, set to 15 by default. An option permits the initialization of this fixed point algorithm with the displacement returned by the DIS optical flow algorithm to reduce computing time. Moreover, when solving Eq. (4), the current phase modulation is interpolated at the location given by the iteratively-estimated displacement $\underline{u}^{\mathrm{it}}$, *i.e.* $(\varphi_\ell^t(\underline{\mathrm{x}} + \underline{u}^{\mathrm{it}}(\underline{\mathrm{x}})))_{\ell\in\{\alpha,\beta\}}$. Since the region of interest is defined in the reference state, for pixels close to its boundary, the zero initial guess of the displacement, *i.e.* $\underline{u}^{\mathrm{it}=0}$, might lead to interpolating the current phase at a point of the image which does not correspond anymore to the specimen surface. Initializing the `compute_displacement` method with the displacement returned by the DIS optical flow algorithm also prevents such an issue.

2.4. Software functionalities

The proposed code computes phase modulations of two orthogonal wave carriers within a pair of images. It deduces the displacement field from these phase modulations. The properties of the pattern ($\underline{k}_\alpha$ and $\underline{k}_\beta$) and the LSA parameters (wave vectors characterizing the pattern periodicity) are automatically computed. Two additional functionalities are introduced at this stage. They are discussed in the next two sections.

2.4.1. Phase and phases classes

The code introduces two additional classes related to the phase modulation quantity to facilitate its use. A phase modulation corresponds to the pixel-wise shift of an imaged pattern to its theoretical wave carrier. The `Phase` class encapsulates this information: its attributes include the wave carrier, defined by its wave vector denoted `vec_k`, and the phase modulation, formatted as a Numpy array and called `data`. An additional attribute corresponds to the dimensions of the `data` array. Several methods are defined within the `Phase` class. For example, the `unwrap` and `interp` methods spatially unwrap and interpolate the phase maps, respectively. Additionally, the `save` and `load` methods aid in backing up results using the `npz` Numpy compressed file format.

The `Phases` class primarily consists of a list of objects defined as instances of the `Phase` class. Applying the main methods, such as `unwrap` and `interp`, of the `Phase` class to an object of the `Phases` class propagates them to each phase it encapsulates. Since images contain two phase modulations, one for each wave carrier, manipulating objects of the `Phases` class greatly enhances the ease of code reading.

2.4.2. Reducing sensor noise effect considering an image stack

An additional method called `compute_refstate_from_im_stack` is proposed for computing an averaged reference phase modulation from a stack of images. Indeed, it is often recommended to acquire several pictures of the unloaded reference state to minimize the impact of sensor noise on displacement estimation. Nevertheless, directly averaging the pictures may potentially result in a biased estimation of the noiseless reference phase map. Indeed, micro-vibrations (if any) occurring while capturing the stack of reference images can induce a bias in the phase map of the resulting averaged reference image. Here, the phase modulation is computed for each image of the stack, and the rigid body motion with respect to the first image of this stack is estimated and removed. A consistent average phase modulation is then computed.

The available images are also used to compute the noise floor level associated with the proposed measurement. For this purpose, the displacement and the strain fields that warp the first image to each other images in the stack are computed using the aforementioned phase modulations. This allows the estimation of the metrological performance of the measurement tool:

- The standard deviation of each component of the displacement and strain is calculated pixel-wise. The input variable `display` of the `compute_refstate_from_im_stack` method can be set to `True` for displaying such standard deviation maps. The global standard deviation of each component is also computed. It defines the measurement resolution [58]. These values are directly displayed in the terminal.
- The spatial resolution is also computed. The spatial resolution corresponds here to the smallest period of a sine displacement measured with a bias equal to $\lambda\%$ or less. Here, $\lambda = 10\%$ to be consistent with other studies dealing with the metrological performance of full-field measurement techniques [33,38,44]. The closed form expression of this quantity given in [59] is used here.
- The Metrological Efficiency Indicator (MEI) [60] is finally estimated for the displacement and the strain. For both quantities, only the component of the maximal measurement resolution is kept for calculating an upper bound.

Since the first image of the stack defines the reference coordinate system for the averaged phase modulations, it must also be used to initialize the problem for further LSA calculations. To avoid misuse, the `compute_refstate_from_im_stack` method runs the OpenLSA constructor with the first image and returns it, along with the calculated reference phase modulations and the kernel employed for it.

2.4.3. Access to image stored on an s3 server

In our research institute, data are stored in a lasting manner using an s3 server. For this purpose, OpenLSA code is written in such a way that access to an image stack is possible when an `s3_dictionary` is provided. This option is especially implemented for the OpenLSA constructor, which can thus build a reference phase from images stored in a single folder in such a s3 server.

3. Illustrative examples

3.1. Highlights of the main OpenLSA features

As a typical example, the OpenLSA software is applied here to images obtained during a compression test of a wood specimen. The images have already been used for another purpose in [52]. The specimen is made of fir, with dimensions of $50 \times 35 \times 15$ [mm^3]. It is subjected to a load of 955 [N], see picture in Fig. 4(a). A checkerboard pattern was deposited on the observed surface of the specimen with the procedure detailed in [61]. It is worth noting that since then, the marking procedure has been simplified by using a laser engraver [47]. The deposited pattern features squares 100 [µm] wide. It is encoded with a 12-bit Sensicam CCD camera featuring 1376×1040 pixels, see the reference image I^0 in Fig. 4(b). The close-up view in Fig. 4(c) displays the white and black squares.

First, the properties of the wave carriers are computed. For illustration, the Discrete Fourier Transform is applied to the image I^0. The resulting spectrogram is depicted in Fig. 4(d). According to the details provided in Section 2, a portion of this representation is masked to estimate a preliminary wave vector. This mask is displayed with a reduced transparency in Fig. 4(d). Both the $\underline{k}_\alpha$ and $\underline{k}_\beta$ wave vectors are plotted in Fig. 4(e), which is a close-up view of the spectrogram of image I^0.

In this example, the standard deviation of the Gaussian window used in LSA is set to its minimum value, *i.e.*, the pattern period. This length corresponds here to the minimum distance between two black or white squares obtained on the diagonal of the squares. It is then possible to extract the phase modulations from the reference image along both the $\underline{e}_\alpha$ and $\underline{e}_\beta$ directions at the frequency of $\|\underline{k}_\ell\|$. They are illustrated in Figs. 5(a) and 5(b). These figures also show the automatic selection of the region of interest, which considers all the pixels for which the modulus is greater than 25% of its maximum value. The pixels not included within this region of interest are not displayed. If any, they appear in white in Figs. 5(a) and 5(b) and in all subsequent Figures.

As discussed in Section 2, the raw estimation of the phase maps is computed pixelwise and *modulo* 2π. The resulting raw phase maps are unwrapped, and the results are shown in Figs. 5(c) and 5(d). The same procedure is then applied to the current image I^t. The corresponding unwrapped phases are shown in Figs. 5(e) and 5(f). The temporal pairing with the reference image I^t has been achieved through the calculation of the movement that followed an arbitrary point $\underline{x}_0$ located at the coordinates $[867, 412]$, as indicated by a red cross in Fig. 4(b). This point corresponds to a feature, illustrated in Fig. 6, easily trackable from one image to another.

Finally, the displacement maps along directions 1 and 2 are deduced from the two phase modulations, according to Eq. (4). They are plotted in Fig. 7(e).

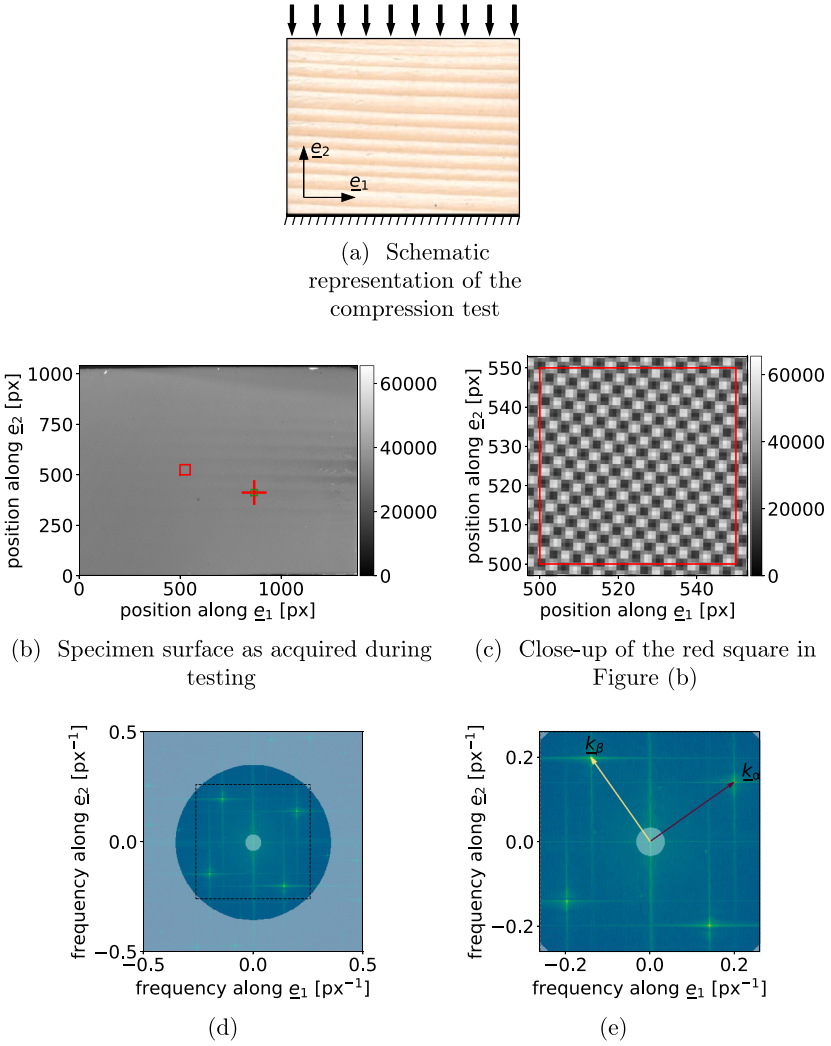

(a) Schematic representation of the compression test

(b) Specimen surface as acquired during testing

(c) Close-up of the red square in Figure (b)

(d)

(e)

Fig. 4. Illustrative example: (a) Wood specimen subjected to compression test. (b) Image of the specimen surface after depositing a checkerboard pattern. (c) Close-up view of this pattern. (d) Spectrogram of the image is shown in (b); transparency is added to highlight the masked area where peaks are not searched. (e) Central part of (a), with superposition of both the wave vectors $\underline{k}_\alpha$ and $\underline{k}_\beta$.

The strain maps are displayed in Fig. 7(e). The following remarks can be drawn from this Figure:

- As expected with this kind of test, the order of magnitude of the strain is quite small. Indeed, the longitudinal strain ε_{22} remains below 1%, in absolute value (see Fig. 7(d)). In other words, the difference in displacement is about 1 pixel between the top and bottom of the specimen.
- ε_{11} of Fig. 7(c) illustrates the Poisson effect. With a mean value of about 2.4×10^{-4} [-], ε_{11} reveals the effect of sensor noise propagation on the strain maps. Interestingly, the strain noise observed here does not correlate with the pattern, contrary to its counterpart observed with DIC [35,36] in similar cases.
- Because it processes optimized patterns, LSA provides displacement/strain maps with the highest possible metrological performance. This is highlighted by the ability of the method to illustrate material heterogeneity within strain maps. Here, early and late woods are identifiable in the strain maps. This is particularly true for the normal strain ε_{22}, and the shear strain ε_{12}; see Figs. 7(c) and 7(e).

3.2. Using an image stack of the reference state for improving metrological performance

The second example illustrates the ability of the OpenLSA program to take advantage of an image stack of the reference state to improve the metrological performance of the measurement. For this purpose, a set of images already used in [62] and available here [63] are employed. These images correspond to a tensile test of a wood specimen and come from Test #2 of [62]. This test has been selected here because the observed strain maps are of low level and consequently show a relatively poor signal-to-noise ratio. A checkerboard pattern has been deposited onto the wood surface following the procedure presented in [47]. An interested reader will find more details about the test in [62].

Images have been duplicated onto our university's s3 server to facilitate code testing, example manipulation, and the illustration of the s3 access code option. Moreover, images are cropped to 1024 × 1024 pixels to reduce the computing time of this illustration. The crop location includes a few tree rings, which induce strain map heterogeneity to emphasize the gain of using an image stack. Two sets of images are available:

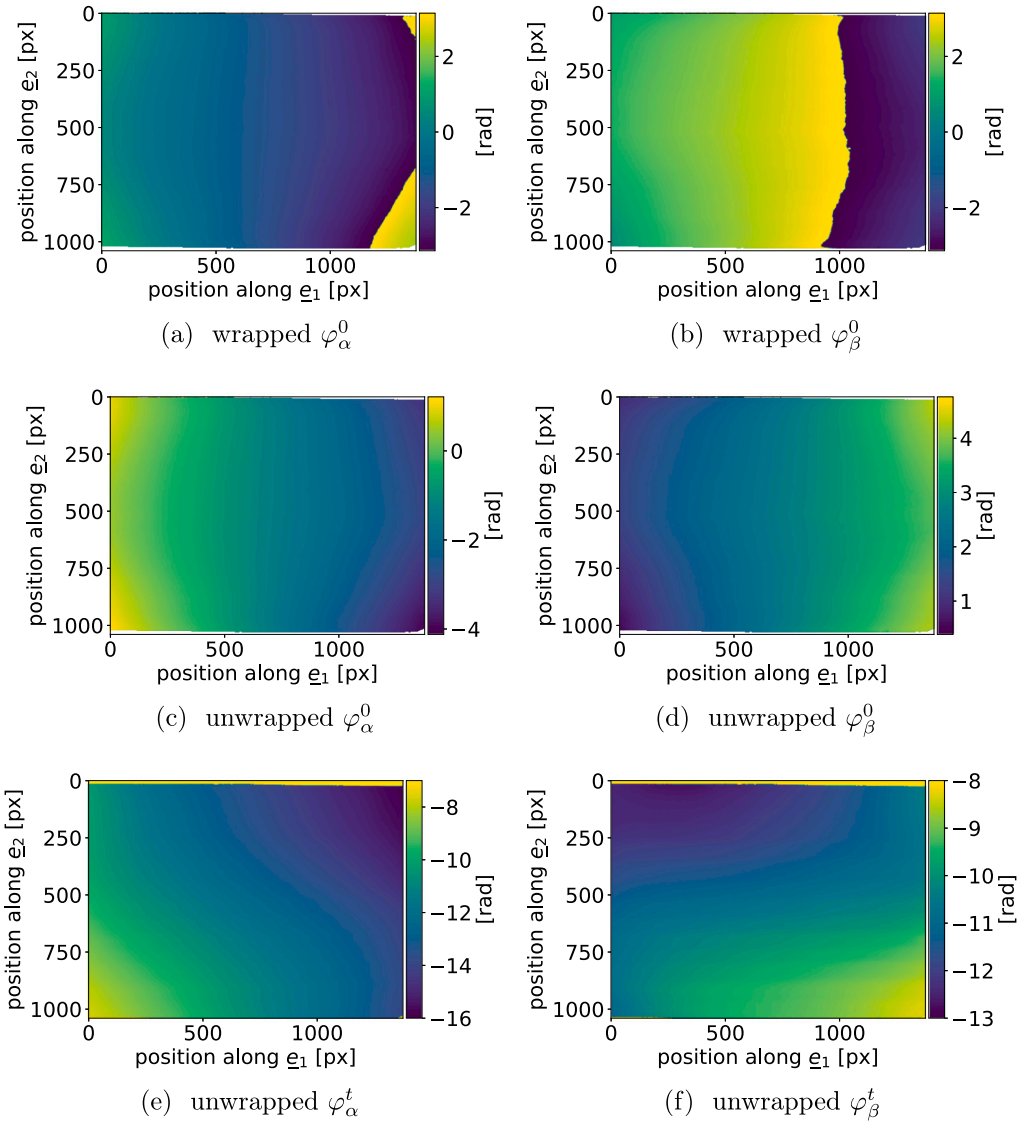

Fig. 5. Phase maps associated with images I^0 and I^t (a) and (b) are the raw phase maps associated with image I^0 along the wave carrier directions: (a) (resp. (b)) corresponds to the carrier of wave vector $\underline{k}_\alpha$ (resp. $\underline{k}_\beta$). The results are wrapped because they are given *modulo* 2π. (c) and (d) show the same phase maps after unwrapping. (e) and (f) display the unwrapped phase maps associated with image I^t.

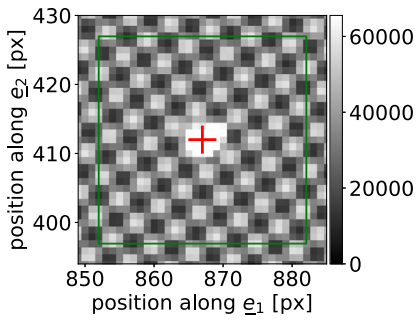

Fig. 6. Close-up of the green square in Fig. 4(b), which is centered on a specific pattern feature. The later is tracked across images to solve the phase modulations' temporal pairing.

- the first set is called $\mathcal{I}^0$ and contains 201 images corresponding to the reference state (loading $F = 0$ [N]): $\mathcal{I}^0 = (I^0_t)_{t\in\{0,\dots,200\}}$;
- the second set, called $\mathcal{I}^1$, was exceptionally taken to capture the current state (loading $F = 3200$ [N]). It collects 201 images: $\mathcal{I}^1 = (I^1_t)_{t\in\{0,\dots,200\}}$.

Three image procedures are applied to these sets.

- First, LSA is applied using only the first image of each set. Let $\underline{u}^{1\ im}$ be the retrieved displacement. This displacement corresponds to the regular use of LSA, which relies on a pair of images.
- LSA is then applied using the whole set $\mathcal{I}^0$ and the first image of the $\mathcal{I}^1$ set. The obtained displacement is denoted by $\underline{u}^{im\ stack}$. It corresponds to the proposed strategy, in which an image stack of the reference state is taken to improve the metrological performance, and one current image is indeed used to describe the current state. Processing the $\mathcal{I}^0$ image set, which corresponds to multiple views of the same material state, allows the calculation of the metrological performances in this case. The values are given in Table 1.
- Finally, the unusual fact that an image stack of the current state is also available makes the calculation of a noise-reduced current

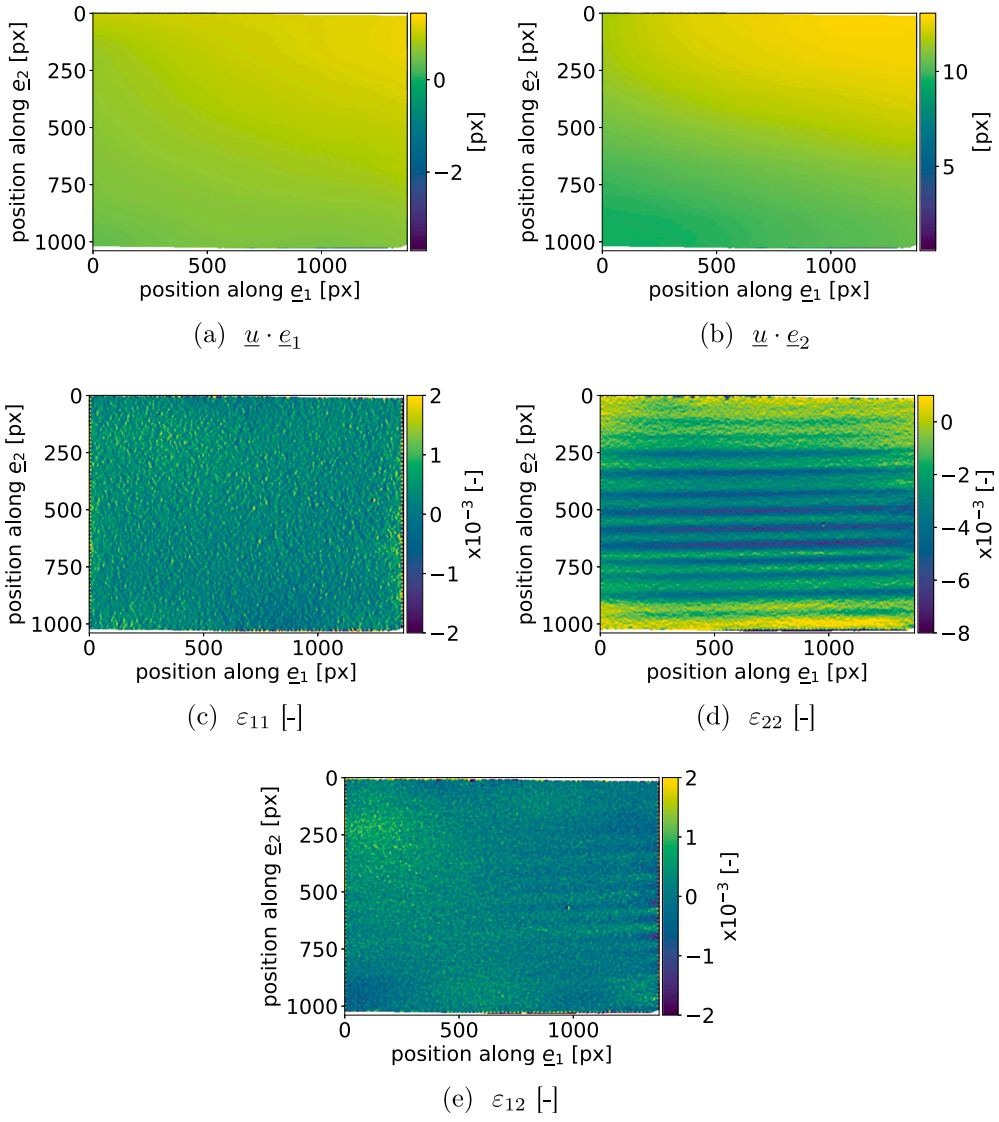

Fig. 7. (a) And (b) are respectively the $\underline{e}_1$ and $\underline{e}_2$ components of the displacement. (c), (d), and (e) are the components of the strain tensor in the $(\underline{e}_1, \underline{e}_2)$ plane. ε_{22} corresponds to the longitudinal strain along direction 2. This is a compression test, so ε_{22} is negative.

Table 1
Expected metrological performances estimated with the image stack used to calculate the reference phase.

Name	Component	Value
Measurement resolution	u_1	4.37×10^{-3} [px]
	u_2	4.85×10^{-3} [px]
	ϵ_{11}	5.24×10^{-4} [–]
	ϵ_{22}	5.28×10^{-4} [–]
	ϵ_{12}	3.71×10^{-4} [–]
Spatial resolution	–	55.3 [px]
Metrological efficiency indicator (MEI)	displacement	0.27 [px^2]
	strain	1.62 [px]

phase possible. The `compute_refstate_from_im_stack` method is thus run for this purpose. A displacement is then deduced from both the reference and the current noise-reduced phases; it is denoted by $\underline{u}^{nr}$. In what follows, the latter is used to characterize the measurement error associated with $\underline{u}^{1\ im}$ and $\underline{u}^{im\ stack}$.

The focus is made here on the strain maps, on which the effect of noise is clearly noticeable. Fig. 8 gathers the results. Fig. 8(a) shows $\epsilon_{22}^{1\ im} = \varepsilon_{22}(\underline{u}^{1\ im})$ maps. On top of the tree rings, the usual peach-skin aspect of the noise is visible. The latter is indeed perceptible for strain values of a few 10^{-3}. The standard deviation of the error between the 22–strain maps elaborated from $\underline{u}^{1\ im}$ and $\underline{u}^{nr}$ is equal to 8.78×10^{-4} [px].

Fig. 8(b) shows $\epsilon_{22}^{im\ stack} = \varepsilon_{22}(\underline{u}^{im\ stack})$. Tree rings are also visible, and the map is slightly less noisy. The standard deviation of the error between the 22–strain maps elaborated from $\underline{u}^{im\ stack}$ and $\underline{u}^{nr}$ is equal to 6.06×10^{-4} [px].

By definition, the variance of the strain maps is proportional to the average of the variances of the phases of the reference and the current states [59]. When a large image stack is considered for estimating the reference phase, the latter can be considered as noiseless. Consequently, the variance of the strain maps should be divided by 2, and thus its standard deviation by $\sqrt{2}$. This property is almost verified here:

$$\frac{\mathrm{std}(\epsilon_{22}^{1\ im} - \epsilon_{22}^{nl})}{\mathrm{std}(\epsilon_{22}^{im\ stack} - \epsilon_{22}^{nl})} = \frac{8.78 \times 10^{-4}}{6.06 \times 10^{-4}} = 1.45 \approx \sqrt{2}. \tag{9}$$

Finally, Fig. 8(c) plots the $\epsilon_{22}^{1\ im}$ and $\epsilon_{22}^{im\ stack}$ strains along the line shown in Fig. 8(a) (black line) and Fig. 8(b) (red line), respectively.

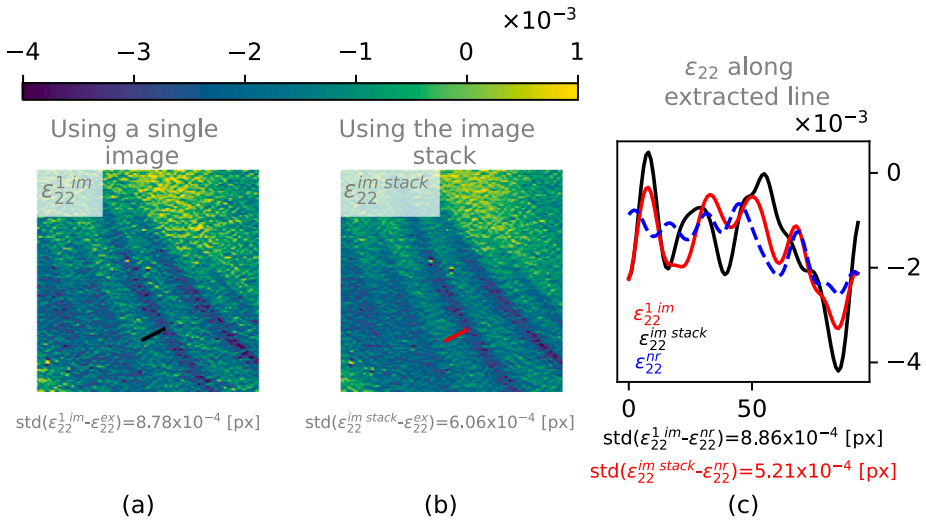

Fig. 8. 22-Strain maps obtained (a) using a pair of images which correspond to the reference and the current states, (b) using an image stack for the reference state and a single image for the current state. Extraction of the data along the black line (a) and red line (b). The dashed blue line corresponds to noise-reduced strain data elaborated using image stacks for both the reference and the current states. Standard deviations are computed with respect to this noise-reduced strain. (For interpretation of the references to color in this figure legend, the reader is referred to the web version of this article.)

The dashed blue line corresponds to ε_{22}^{nr} at the same location. Again, $\varepsilon_{22}^{im\ stack}$ is closer to ε_{22}^{nr}. This is confirmed by the standard deviation of the difference $\varepsilon_{22}^{1\ im} - \varepsilon_{22}^{nr}$ and $\varepsilon_{22}^{im\ stack} - \varepsilon_{22}^{nr}$ along this line:

$$\mathrm{std}(\varepsilon_{22}^{1\ im} - \varepsilon_{22}^{nl}) = 8.86 \times 10^{-4} > 5.21 \times 10^{-4} = \mathrm{std}(\varepsilon_{22}^{im\ stack} - \varepsilon_{22}^{nl}) \qquad (10)$$

4. Impact

Material comprehension and optimization are significant motivations for many studies in the experimental mechanics community. Undoubtedly, full-field measurement techniques have revolutionized how experimentalists perceive their experiments. Material testing is currently undergoing a breakthrough, with experimentation designed to leverage the rich insights provided by full-field measurements [64,65]. Thanks to its availability as commercial or free software, Digital Image Correlation (DIC) is routinely used for computing displacement and strain fields. However, DIC has drawbacks, such as its inability to deal with patterns optimized for metrological performance. Localized Spectrum Analysis (LSA), the backbone of OpenLSA, is specifically designed to process such optimal patterns, such as checkerboards. While an early in-house Matlab software toolbox is available [54], by publishing our Python code, we aim to assist DIC users and experimentalists in exploring the alternative offered by the LSA method. The outstanding metrological performance of LSA [43] ensures its valuable use.

The deposition of patterns was previously a challenge that limited the adoption of LSA. However, this limitation is now outdated, thanks to the ease of use of a laser engraver [47], and more recently, the ability to deposit checkerboard patterns using similar materials and techniques as those used for strain gauges [62].

We aim to contribute to the broader scientific community by sharing our methods, techniques, and findings, in the hope that they will assist other researchers in understanding and potentially building upon our work.

Moreover, LSA has facilitated collaborations for us, both at a national level [51,66] and internationally [46,49,50,67]. Making this code accessible will contribute to the dissemination of these relevant full-field measurement techniques in the experimental mechanics community, serving as a valuable resource for experimentalists tackling similar problems or building upon related concepts. Additionally, the software code is intended for educational purposes.

Making our research publicly available also enhances its reproducibility. Other researchers can now utilize and validate our methods, leading to more robust and reliable scientific results.

Finally, this work contributes to the ongoing efforts aimed at standardizing full-field measurement techniques, particularly in surface marking. The geometry of a periodic pattern, such as a checkerboard, can be easily defined with a limited number of parameters, making it conducive to standardization.

5. Conclusions

In this article, we introduce OpenLSA, a software that applies Localized Spectrum Analysis (LSA) to images of periodic patterns to retrieve the displacement that warps them. LSA demands low computations. It processes optimal patterns, such as checkerboard patterns, and provides full-field measurements with the best metrological performance. Dedicated to the experimental mechanics community, this program will significantly facilitate the adoption of LSA. Written as a Python class, its use is easy, with many automated steps. Thanks to its open-source nature, it encourages community collaboration.

Further work will propose integrating the dedicated deconvolution algorithm for LSA, which will enhance the metrological performance of the measuring tool. Lastly, an additional extension that would enhance the framework's usability is the integration of a camera model to take it into account within full-field estimation.

CRediT authorship contribution statement

Benoît Blaysat: Writing – review & editing, Writing – original draft, Visualization, Validation, Software, Methodology, Investigation, Funding acquisition, Formal analysis, Conceptualization. **Frédéric Sur:** Writing – review & editing, Writing – original draft, Software, Methodology, Formal analysis, Conceptualization. **Thomas Jailin:** Writing – review & editing, Writing – original draft, Software, Methodology. **Adrien Vinel:** Writing – review & editing, Writing – original draft, Software, Methodology. **Michel Grédiac:** Writing – review & editing, Writing – original draft, Methodology, Formal analysis, Conceptualization.

Declaration of competing interest

The authors declare the following financial interests/personal relationships which may be considered as potential competing interests: BENOIT BLAYSAT reports financial support was provided by Université Clermont Auvergne. If there are other authors, they declare that they have no known competing financial interests or personal relationships that could have appeared to influence the work reported in this paper.

Data availability

Data is linked (https://github.com/BenoitBlaysat/OpenLSA.git).

Acknowledgments

The authors acknowledge support from the French government research program “Investissements d’Avenir” through the IDEX-ISITE initiative 16-IDEX-0001 (CAP 20-25) and the AURA regional council.

References

[1] Sutton MA, Orteu JJ, Schreier H. Image correlation for shape, motion and deformation measurements: basic concepts, theory and applications. Springer; 2009, http://dx.doi.org/10.1007/978-0-387-78747-3.
[2] Passieux JC, Fouque R. pyxel. 2023, URL https://zenodo.org/records/7793940.
[3] Seghir R, Witz J-F, Coudert S. yadics. 2012, URL https://yadics.univ-lille1.fr/wordpress/index.html.
[4] Blaber J, Adair B, Antoniou A. Ncorr: Open-source 2d digital image correlation matlab software. Exp Mech 2015;55(6):1105–22. http://dx.doi.org/10.1007/s11340-015-0009-1.
[5] Turner DZ. Digital image correlation engine (dICe) reference manual. Tech. rep. SAND2015-10606, Sandia; 2015, URL https://github.com/dicengine/dice.
[6] Matchid. 2024, URL https://www.matchid.eu.
[7] Correlated solutions. 2024, URL https://www.correlatedsolutions.com/vic-3d.
[8] Eikosim. 2024, URL https://eikosim.com/validation-simulations/.
[9] Champagnat F, Plyer A, Besnerais GL, Leclaire B, Davoust S, Sant YL. Fast and accurate piv computation using highly parallel iterative correlation maximization. Exp Fluids 2011;50. http://dx.doi.org/10.1007/s00348-011-1054-x.
[10] Couty V, Witz J-F, Lecomte-Grosbras P, Berthe J, Deletombe E, Brieu M. GPU-Correl: A GPU accelerated Digital Image Correlation software written in Python. SoftwareX 2021;16:100815. http://dx.doi.org/10.1016/j.softx.2021.100815.
[11] Boukhtache S, Abdelouahab K, Bahou A, Berry F, Blaysat B, Grédiac M, et al. A lightweight convolutional neural network as an alternative to DIC to measure in-plane displacement fields. Opt Lasers Eng 2023;161(107367). http://dx.doi.org/10.1016/j.optlaseng.2022.107367, arXiv:hal-03897689v1.
[12] Boukhtache S, Abdelouahab K, Berry F, Blaysat B, Grédiac M, Sur F. When deep learning meets digital image correlation. Opt Lasers Eng 2020;136(106308). http://dx.doi.org/10.1016/j.optlaseng.2020.106308, arXiv:hal-02933431.
[13] Schreier HW, Sutton MA. Systematic errors in digital image correlation due to undermatched subset shape functions. Exp Mech 2002;42(3):303–10. http://dx.doi.org/10.1007/BF02410987.
[14] Wang YQ, Sutton MA, Bruck HA, Schreier HW. Quantitative error assessment in pattern matching: Effects of intensity pattern noise, interpolation, strain and image contrast on motion measurements. Strain 2009;45(2):160–78. http://dx.doi.org/10.1111/j.1475-1305.2008.00592.x.
[15] Lava P, Cooreman S, Coppieters S, De Strycker M, Debruyne D. Assessment of measuring errors in dic using deformation fields generated by plastic fea. Opt Lasers Eng 2009;47(7):747–53. http://dx.doi.org/10.1016/j.optlaseng.2009.03.007, URL https://www.sciencedirect.com/science/article/pii/S0143816609000451.
[16] Wang YQ, Sutton MA, Ke XD, Schreier HW, Reu PL, Miller TJ. On error assessment in stereo-based deformation measurements. Exp Mech 2011;51(4):405–22. http://dx.doi.org/10.1007/s11340-010-9449-9.
[17] Ke XD, Schreier HW, Sutton MA, Wang YQ. On error assessment in stereo-based deformation measurements. Exp Mech 2011;51(4):423–41. http://dx.doi.org/10.1007/s11340-010-9450-3.
[18] Bossuyt S. Optimized patterns for digital image correlation. In: Proceedings of the 2012 annual conference on experimental and applied mechanics, vol. 3. 2013, p. 239–48. http://dx.doi.org/10.1007/978-1-4614-4235-6_34.
[19] Pan B, Yu L, Wu D, Tang L. Systematic errors in two-dimensional digital image correlation due to lens distortion. Opt Lasers Eng 2013;51(2):140–7. http://dx.doi.org/10.1016/j.optlaseng.2012.08.012.
[20] Pan B. Bias error reduction of digital image correlation using gaussian pre-filtering. Opt Lasers Eng 2013;51(10):1161–7. http://dx.doi.org/10.1016/j.optlaseng.2013.04.009.
[21] Pan B, Yu L, Wu D. High-accuracy 2d digital image correlation measurements with bilateral telecentric lenses: Error analysis and experimental verification. Exp Mech 2013;53(9):1719–33. http://dx.doi.org/10.1007/s11340-013-9774-x.
[22] Pan B, Xie H, Wang Z. Equivalence of digital image correlation criteria for pattern matching. Appl Opt 2010;49(28):5501–9. http://dx.doi.org/10.1364/AO.49.005501.
[23] Neggers J, Blaysat B, Hoefnagels JPM, Geers MGD. On image gradients in digital image correlation. Internat J Numer Methods Engrg 2016;105(4):243–60. http://dx.doi.org/10.1002/nme.4971.
[24] Wang Y, Lava P, Reu P, Debruyne D. Theoretical analysis on the measurement errors of local 2d dic: Part i temporal and spatial uncertainty quantification of displacement measurements. Strain 2016;52(2):110–28. http://dx.doi.org/10.1111/str.12173.
[25] Su Y, Zhang Q, Xu X, Gao Z. Quality assessment of speckle patterns for dic by consideration of both systematic errors and random errors. Opt Lasers Eng 2016;86:132–42. http://dx.doi.org/10.1016/j.optlaseng.2016.05.019.
[26] Blaysat B, Grédiac M, Sur F. Effect of interpolation on noise propagation from images to DIC displacement maps. Internat J Numer Methods Engrg 2016;108(3):213–32. http://dx.doi.org/10.1002/nme.5212, arXiv:hal-01255944.
[27] Blaysat B, Grédiac M, Sur F. On the propagation of camera sensor noise to displacement maps obtained by DIC - an experimental study. Exp Mech 2016;56(6):919–44. http://dx.doi.org/10.1007/s11340-016-0130-9, arXiv:hal-01269655.
[28] Rossi M, Lava P, Pierron F, Debruyne D, Sasso M. Effect of DIC Spatial Resolution, Noise and Interpolation Error on Identification Results with the VFM. Strain 2015;51(3):206–22. http://dx.doi.org/10.1111/str.12134.
[29] Bomarito GF, Hochhalter JD, Ruggles TJ, Cannon AH. Increasing accuracy and precision of digital image correlation through pattern optimization. Opt Lasers Eng 2017;91:73–85. http://dx.doi.org/10.1016/j.optlaseng.2016.11.005.
[30] Lehoucq RB, Reu PL, Turner DZ. The effect of the ill-posed problem on quantitative error assessment in digital image correlation. Exp Mech 2017. http://dx.doi.org/10.1007/s11340-017-0360-5.
[31] Bornert M, Doumalin P, Dupré JC, Poilâne C, Robert L, Toussaint E, et al. Assessment of digital image correlation measurement accuracy in the ultimate error regime: Improved models of systematic and random errors. Exp Mech 2018;58(1):33–48. http://dx.doi.org/10.1007/s11340-017-0328-5.
[32] Reu PL, Toussaint E, Jones E, Bruck HA, Iadicola M, Balcaen R, et al. Dic challenge: Developing images and guidelines for evaluating accuracy and resolution of 2d analyses. Exp Mech 2018;58(7):1067–99. http://dx.doi.org/10.1007/s11340-017-0349-0.
[33] Blaysat B, Neggers J, Grédiac M, Sur F. Towards criteria characterizing the metrological performance of full-field measurement techniques - application to the comparison between local and global versions of DIC. Exp Mech 2020;60(3):393–407. http://dx.doi.org/10.1007/s11340-019-00566-4, arXiv:hal-02436541.
[34] Passieux J-C, Bouclier R. Classic and inverse compositional Gauss–Newton in global DIC. Internat J Numer Methods Engrg 2019;119(6):453–68. http://dx.doi.org/10.1002/nme.6057.
[35] Sur F, Blaysat B, Grédiac M. On biases in displacement estimation for image registration, with a focus on photomechanics. J Math Imaging Vision 2021;63:777–806. http://dx.doi.org/10.1007/s10851-021-01032-4, arXiv:hal-03226201v1.
[36] Fayad SS, Seidl DT, Reu PL. Spatial DIC errors due to pattern-induced bias and grey level discretization. Exp Mech 2020;60(2):249–63. http://dx.doi.org/10.1007/s11340-019-00553-9.
[37] Fouque R, Bouclier R, Passieux J-C, Périé J-N. Fractal pattern for multiscale digital image correlation. Exp Mech 2021;61(3):483–97. http://dx.doi.org/10.1007/s11340-020-00649-7.
[38] Reu PL, Blaysat B, Andó E, Bhattacharya K, Couture C, Couty V, et al. 2.0: Developing images and guidelines for evaluating accuracy and resolution of 2D analyses. Exp Mech 2022. http://dx.doi.org/10.1007/s11340-021-00806-6, arXiv:hal-03427288v1.
[39] Liu Y, Fang Z, Ren T, Zhao J, Su Y, Zhang Q. Universal method using a pre-deformed reference subset to eliminate the interpolation bias in digital image correlation. Appl Opt 2023;62(34):8968–77. http://dx.doi.org/10.1364/AO.488797.
[40] Ye X, Zhao J. Minimizing the total strain error in point-wise least squares using rotated gaussian weight strain filter (rgw-sf) in digital image correlation. Opt Lasers Eng 2023;164:107492. http://dx.doi.org/10.1016/j.optlaseng.2023.107492.
[41] Shi Y, Blaysat B, Chanal H, Grédiac M. Designing patterns for DIC with Poisson image editing. Exp Mech 2022;62(1093–1117). http://dx.doi.org/10.1007/s11340-022-00862-6, arXiv:hal-03784274v1.
[42] Bomarito GF, Hochhalter JD, Ruggles TJ. Development of optimal multiscale patterns for digital image correlation via local grayscale variation. Exp Mech 2018. http://dx.doi.org/10.1007/s11340-017-0348-1.
[43] Grédiac M, Blaysat B, Sur F. On the optimal pattern for displacement field measurement: random speckle and DIC, or checkerboard and LSA? Exp Mech 2020;60:509–34. http://dx.doi.org/10.1007/s11340-019-00579-z, arXiv:hal-02462030.

[44] Grédiac M, Balandraud X, Blaysat B, Jailin T, Langlois R, Sur F, Vinel A. Fine-tuning a deconvolution algorithm to restore displacement and strain maps obtained with lsa. Exp Mech 2023;63(9):1509–37. http://dx.doi.org/10.1007/s11340-023-00997-0.

[45] Vinel A, Laquet M, Balandraud X, Blaysat B, Grédiac M, Jailin T. Full-field strain investigation of twinned martensite in a thermally activated Cu–Al–Ni single crystal using Localized Spectrum Analysis. Acta Mater 2024;264:119550. http://dx.doi.org/10.1016/j.actamat.2023.119550.

[46] Nitu EL, Diakhaté M, Badulescu C, Grédiac M, Blaysat B, Iordache MD, et al. Analyzing defects and their effects on the strength of a three-layer FSW joint by using X-ray microtomography, Localized Spectrum Analysis, and Acoustic Emission. Mater Charact 2022;190(112069). http://dx.doi.org/10.1016/j.matchar.2022.112069, arXiv:hal-03761312v1.

[47] Bouyra Q, Blaysat B, Chanal H, Grédiac M. Using laser marking to engrave optimal patterns for in-plane displacement and strain measurement. Strain 2022;58(2):e12404. http://dx.doi.org/10.1111/str.12404, arXiv:hal-03541996v1.

[48] Grédiac M, Blaysat B, Sur F. Comparing several spectral methods used to extract displacement fields from checkerboard images. Opt Lasers Eng 2020;127(105984). http://dx.doi.org/10.1016/j.optlaseng.2019.105984, arXiv:hal-02436572.

[49] Blaysat B, Balandraud X, Grédiac M, Vives E, Barrera N, Zanzotto G. Concurrent tracking of strain and noise bursts at ferroelastic phase fronts. Commun Mater 2020;1. http://dx.doi.org/10.1038/s43246-020-0007-4, arXiv:hal-03026020.

[50] Qin S, Grédiac M, Blaysat B, Ma S, Sur F. Influence of the sampling density on the noise level in displacement and strain maps obtained by processing periodic patterns. Measurement 2020;173:108570. http://dx.doi.org/10.1016/j.measurement.2020.108570.

[51] Langlois R, Cusset R, Hosdez J, Bonnand V, Blaysat B, Menut-Tournadre L, et al. Multi-partner benchmark experiment of fatigue crack growth measurements. Eng Fract Mech 2020;235:107157. http://dx.doi.org/10.1016/j.engfracmech.2020.107157, arXiv:hal-02877391.

[52] Grédiac M, Blaysat B, Sur F. A robust-to-noise deconvolution algorithm to enhance displacement and strain maps obtained with local DIC and LSA. Exp Mech 2019;59(2):219–43. http://dx.doi.org/10.1007/s11340-018-00461-4, arXiv:hal-01926058.

[53] Grédiac M, Blaysat B, Sur F. Extracting displacement and strain fields from checkerboard images with the Localized Spectrum Analysis. Exp Mech 2019;59(2):207–18. http://dx.doi.org/10.1007/s11340-018-00439-2, arXiv:hal-01926054.

[54] Grédiac M, Blaysat B, Sur F. Matlab software toolbox of the Grid Method. URL https://members.loria.fr/FSur/software/gridmethod/.

[55] Sur F, Grédiac M. Towards deconvolution to enhance the Grid Method for in-plane strain measurement. Inverse Probl Imaging 2014. http://dx.doi.org/10.3934/ipi.2014.8.259.

[56] Sur F, Grédiac M. Influence of the analysis window on the metrological performance of the grid method. J Math Imaging Vision 2016;56(3):472–98. http://dx.doi.org/10.1007/s10851-016-0650-z.

[57] Reu P. All about speckles: Aliasing. Exp Tech 2014;38(5):1–3. http://dx.doi.org/10.1111/ext.12111.

[58] JCGM Member Organizations. International vocabulary of metrology – Basic and general concepts and associated terms (VIM), vol. 200. BIPM; 2012.

[59] Grédiac M, Sur F. Effect of sensor noise on the resolution and spatial resolution of displacement and strain maps estimated with the grid method. Strain 2014;50(1):1–27.

[60] Grédiac M, Blaysat B, Sur F. A critical comparison of some metrological parameters characterizing local digital image correlation and Grid Method. Exp Mech 2017;57(6):871–903. http://dx.doi.org/10.1007/s11340-017-0279-x, arXiv:hal-01509611.

[61] Piro JL, Grédiac M. Producing and transferring low-spatial-frequency grids for measuring displacement fields with Moiré and Grid Methods. Exp Tech 2004;28(4):23–6. http://dx.doi.org/10.1111/j.1747-1567.2004.tb00173.x.

[62] Vinel A, Grédiac M, Balandraud X, Blaysat B, Jailin T, Sur F. Towards strain gauge 2.0. Substituting the electric resistance routinely deposited on polyimide film by the optimal pattern for full-field strain measurement. Strain 2024. [in press].

[63] Vinel A, Grédiac M, Balandraud X, Blaysat B, Jailin T, Sur F. Testing a new optical strain gage for full-field strain measurement: Raw images. 2024, http://dx.doi.org/10.5281/zenodo.11185323, URL https://zenodo.org/doi/10.5281/zenodo.11185323.

[64] Pierron F, Grédiac M. Towards Material Testing 2.0. a review of test design for identification of constitutive parameters from full-field measurements. Strain 2021;57(1):e12370. http://dx.doi.org/10.1111/str.12370.

[65] Pierron F. Material testing 2.0: A brief review. Strain 2023;59(3):12434. http://dx.doi.org/10.1111/str.12434, URL https://onlinelibrary.wiley.com/doi/abs/10.1111/str.12434.

[66] Tixier D, Blaysat B, Fourest T, Grédiac M, Langrand B, Berthe J, et al. Using a high-resolution full-field measurement technique to study heterogeneous strain fields obtained during an off-axis test on T700gc/M21 unidirectional composite. In: British society of strain measurement. 2023.

[67] Jongchansitto K, Balandraud X, Blaysat B, Grédiac M, Jailin T, Le Cam J-B, et al. Measuring forces in a 2D multi-contact system using the Virtual Fields Method: principle, simulations and experimental application to a three-particle system. 2024, [in revision].